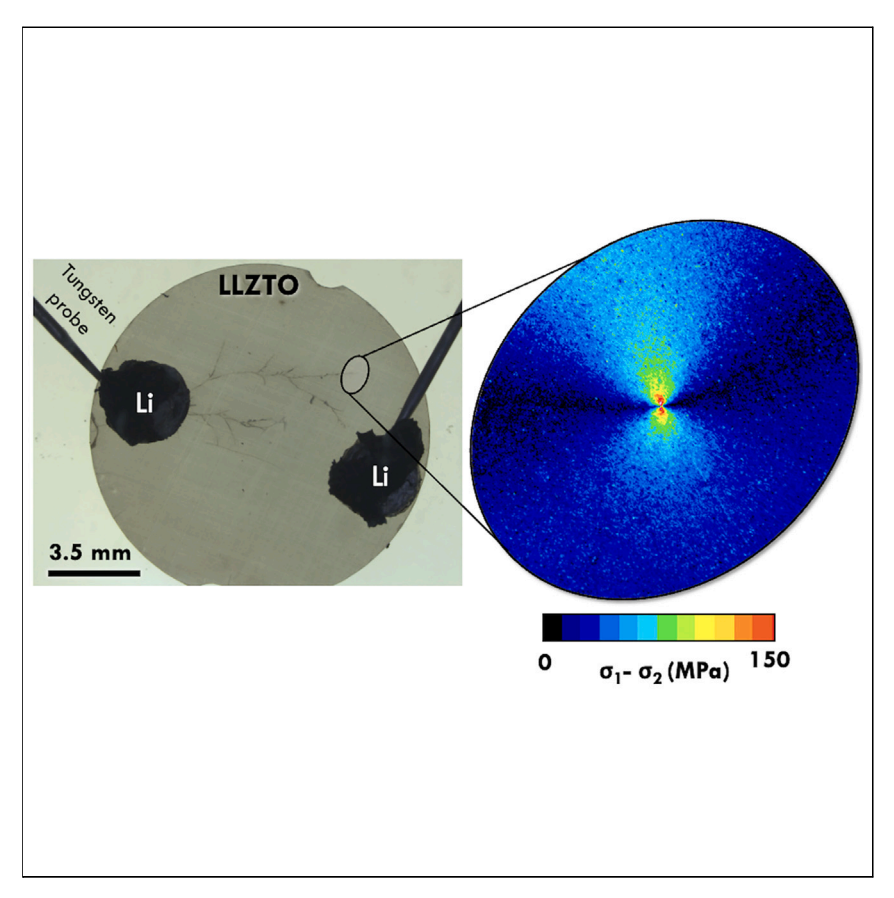
Matter



Article

Operando measurements of dendrite-induced stresses in ceramic electrolytes using photoelasticity



This study introduces a method to directly measure stress fields in solid electrolytes—a long-standing challenge in battery research—using the principle of photoelasticity. In the study, the first direct measurements of stress around lithium dendrites within a garnet electrolyte are presented. The findings align with theoretical predictions for stress fields of internally pressurized cracks in elastic media. The innovative experimental platform holds promise for illuminating diverse chemo-mechanical failures in solid-state batteries, heralding a new era in contactless battery diagnostics.

Christos E. Athanasiou, Cole D. Fincher, Colin Gilgenbach, Huajian Gao, W. Craig Carter, Yet-Ming Chiang, Brian W. Sheldon

athanasiou@gatech.edu (C.E.A.) cfincher@mit.edu (C.D.F.) ychiang@mit.edu (Y.-M.C.) brian_sheldon@brown.edu (B.W.S.)

Highlights

Operando stress measurements during the cycling of solid-state batteries

Direct measurements of stress fields around dendrites

Photoelasticity provides a means to investigate complex chemomechanical events

Athanasiou et al., Matter 7, 95–106 January 3, 2024 © 2023 Elsevier Inc. https://doi.org/10.1016/j.matt.2023.10.014



Matter



Article

Operando measurements of dendrite-induced stresses in ceramic electrolytes using photoelasticity

Christos E. Athanasiou,^{1,2,6,7,*} Cole D. Fincher,^{3,6,*} Colin Gilgenbach,³ Huajian Gao,^{1,4,5} W. Craig Carter,³ Yet-Ming Chiang,^{3,*} and Brian W. Sheldon^{1,*}

SUMMARY

Fundamental understanding of stress buildup in solid-state batteries is elusive due to the challenges in observing electro-chemomechanical phenomena inside solid electrolytes. In this work, we address this problem by developing a method to directly measure stresses within solid-state electrolytes. As a proof-of-concept, we provide the first direct measurements of the stress fields generated around the lithium metal dendrites in a model garnet electrolyte, Li_{6.75}La₃Zr_{1.75}Ta_{0.25}O₁₂, and show that these are consistent with the predictions for an internally loaded crack in an elastic solid. The measurements are based on employing the principle of photoelasticity to probe the stress fields during operando electrochemical cycling in a plan-view cell. This new experimental methodology provides a means to access chemo-mechanical events in solid-state batteries and has the potential to provide insight into a variety of chemo-mechanical failure modes.

INTRODUCTION

Solid-state batteries can potentially provide increased energy density and safety. ^{1,2} However, their performance and durability is often limited by stress-induced chemo-mechanical failure. ^{3–9} Recent work on all-solid-state composite cathodes has shown that stress buildup and subsequent cracking of cathode and electrolytes play a major role in cell failure. ^{10–14} On the anode side, where a metal electrode provides the highest energy densities, an array of studies have hypothesized that plating-induced stress can fracture otherwise-stable solid electrolytes, ^{15–30} based largely upon the dendrite morphology and/or low fracture of toughness solid electrolytes. Thus, directly probing the stress fields inside a battery during cycling can provide critically important information about dendrite growth and a variety of other chemo-mechanical phenomena. However, because these phenomena occur within solid-state cells and involve brittle materials, direct observations are extremely challenging with commonly used research techniques.

To directly investigate chemo-mechanical processes, we develop a method based on the use of photoelasticity to image stress fields in a solid electrolyte. The observations reported were collected during Li plating through a model solid electrolyte, Li_{6.75}La₃Zr_{1.75}Ta_{0.25}O₁₂ (LLZTO). By conducting photoelastic observations in a planview cell, the stress field was examined in the vicinity of a dendrite. Our observations reveal strong agreement between the observed stress field and the predictions of linear elastic fracture mechanics.

More broadly, this study demonstrates that photoelasticity is capable of providing *operando* stress measurements during the cycling of solid-state batteries and can provide a platform to characterize a wide range of chemo-mechanical phenomena.

PROGRESS AND POTENTIAL

Chemo-mechanical phenomena impact the cyclability of solidstate batteries. While conventional Li-ion cells require constant ionic contact between active components, the rigid nature of solid-solid interfaces presents new challenges for maintaining mechanical contact. The loss of mechanical contact at interfaces leads to cell failure. Both cathodes and anodes undergo stress during cycling, potentially fracturing the solid electrolyte. In addition, dendrite growth induces stresses within the electrolyte, affecting degradation and cell lifespan. Despite their importance, no direct stress measurements inside solid electrolytes during cycling have been made due to experimental challenges. To overcome this, a photoelasticity-based platform was created, allowing stress analysis near chemo-mechanical events and aiding in studying battery material failures at varied scales.







RESULTS AND DISCUSSION

Operando stress measurements via photoelasticity

Photoelasticity measurements rely on stress-induced anisotropy in a material. 31-37 More specifically, applied stress creates an anisotropy in the dielectric permittivity, resulting in varying propagation velocities of optical waves polarized along two mutually orthogonal principal directions. This effect makes it possible to determine the difference in maximum principal stresses ($\sigma_1 - \sigma_2$) in a material by measuring optical retardance and applying the stress-optic law.³¹ By applying this method to a solid electrolyte (LLZTO) during lithium plating, our experiments show that it is possible to directly map stresses in the vicinity of a stationary or propagating lithium metal dendrite. To perform photoelasticity measurements operando, we combined the experimental configurations developed in our prior work.^{27,36} A lithium metal electrode is adhered to the electrolyte, as shown in Figure 1B. Two tungsten probes are positioned, one on the lithium metal electrode and one directly in contact with the thinly polished disk of LLZTO.²⁷ The lithium dendrites then form through the thickness of the electrolyte. In Figures 1D-1F, this type of dendrite is propagating in the x-y plane. The propagation of the dendrite is then tracked with an optical microscope fitted with a commercial system to measure optical retardance, which is then used to calculate the stress state (more information in the experimental procedures).36

The experiments, performed in transmission, are facilitated by the use of LLZTO specimens thinned to the point of translucency. The measurements give through-thickness-averaged retardance (i.e., along the z axis in Figure 1C). This method makes it possible to image the stress distribution (within the spatial resolution of the microscope), and thus it provides a direct map of the stress field in the vicinity of a lithium filament. These *operando* experiments, performed while applying a fixed current, give a series of retardance images at different times (Video S1). An example of a false color map of the difference in maximum principal stresses in the vicinity of a dendrite in a 90 μ m thick LLZTO disk is shown in Figure 1F. The stress distribution observed here is in qualitative agreement with photoelasticity measurements obtained in the vicinity of crack tips during fracture. This result confirms that pressure buildup inside of the Li metal-filled filaments produces significant stresses in the solid electrolyte.

The ability to conduct operando photoelasticity measurements provides valuable information about changes that occur during electrochemical cycling. Recent work shows that a variety of dendrite morphologies occur in experiments with this type of configuration (i.e., in-plane propagation of dendrites over several millimeters or more, through a thin LLTZO sheet).²⁷ This includes dendrites that are "leafier" (i.e., more diffuse) than the one shown in Figure 1C, along with branching events that lead to the propagation of multiple dendrites in close proximity. It is challenging to interpret images of these complex morphologies, and thus an isolated dendrite was selected to demonstrate the new photoelasticity method. The observations reported here were thus obtained under conditions where this isolated dendrite dominates. The experiment shown in Figure 1 was selected from several separate experiments with different LLZTO pieces. Dendrite formation occurred in all the experiments, and similar optical retardance patterns and magnitudes were observed. Results for the most isolated dendrite in these experiments is presented here, because it provides detailed quantitative analyses. The filament seen in Figure 2 is the same dendrite imaged in Figure 1C, but subsequent to continued plating at a constant current density of 0.3 mA/cm² (applied current normalized by the electrode/electrolyte interfacial area). The images in Figure 2 show that the retardance

¹School of Engineering, Brown University, Providence, RI 02912, USA

²School of Aerospace Engineering, Georgia Institute of Technology, Atlanta, GA 30332, USA

³Department of Materials Science and Engineering, Massachusetts Institute of Technology, Cambridge, MA 02139, USA

⁴School of Mechanical and Aerospace Engineering, Nanyang Technological University, Singapore 639798, Singapore

⁵Institute of High Performance Computing, A*STAR, Singapore 138632, Singapore

⁶These authors contributed equally

⁷Lead contact

^{*}Correspondence: athanasiou@gatech.edu (C.E.A.), cfincher@mit.edu (C.D.F.), ychiang@mit.edu (Y.-M.C.), brian_sheldon@brown.edu (B.W.S.)





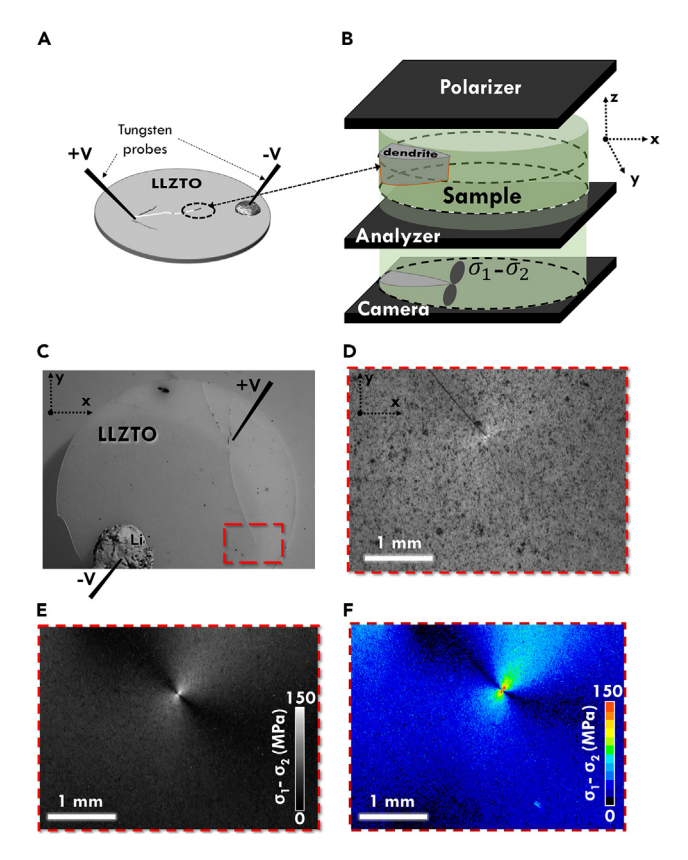


Figure 1. Probing stress operando via photoelasticity

(A–C) Schematic of the experimental setup and the photoelastic principle allowing for measuring the stress field around a metal dendrite—where the stress represents the difference in in-plane maximum principal stresses ($\sigma_1 - \sigma_2$). Metal electrodes adhered to the surface of a thin LLZTO electrolyte and are polarized to produce in-plane metal growth.

- (B) A birefringence microscope measures the corresponding *operando* stress field (see inset) during dendrite growth.
- (C) Post-mortem optical micrograph of a plan-view cell.
- (D) Polarized light image of the red area shown in (C).
- (E and F) Grayscale and false color maps of the difference in principal stresses at the tip of a progressing dendrite. The color bars correspond to the stress levels calculated from the measured retardance maps.

distribution around the dendrite moves as the dendrite propagates with a velocity of $\sim\!\!1~\mu\text{m/s}.$ This clearly demonstrates that the corresponding stress field moves with the dendrite tip.

The position of the dendrite tip can be observed from the polarized optical micrographs (to within the resolution limit of the microscope). The full length of the dendrite is nominally 7 mm based upon Figure 1C, and the advance of the tip from the first to the fourth snapshot is approximately 1.5 mm (Figure 2). For the results in Figure 2, this tip coincides with the maximum retardance intensity. From Figure 2, it can be seen that the tip visible in the polarized light and the retardance images appear coincident.

Analysis

Photoelasticity experiments typically employ the type of configuration used here, with optical transmission through a thin sheet. The optical retardance is then described by: $^{35-37}$





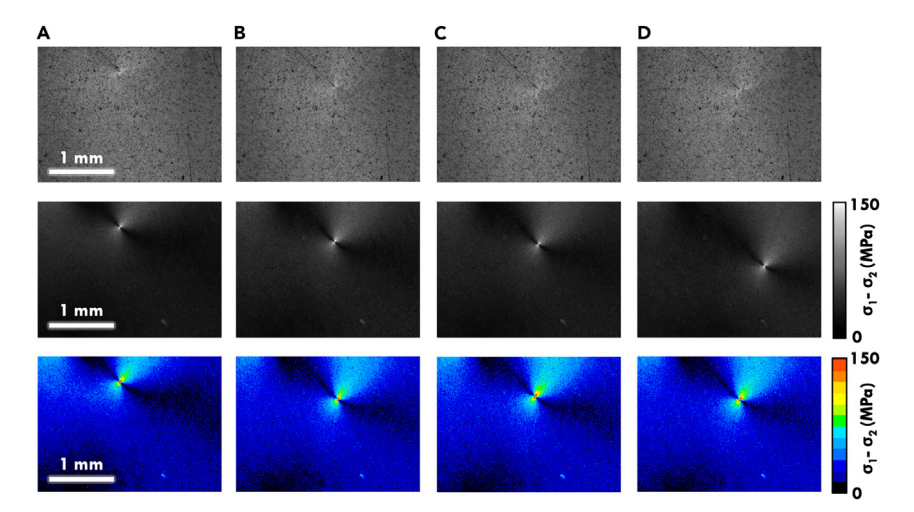


Figure 2. Operando photoelastic maps

(A–D) Operando polarized light micrographs (first row) and the measurements of the difference in principal stresses ($\sigma_1-\sigma_2$, second and third row) recorded during dendrite growth at nominally 0.3 mA/cm². Images depict the region boxed within Figure 1A. Each column corresponds to different snapshots in time. The time interval between the images is ~3 s while the dendrite propagates with a velocity of ~1 μ m/s. The scale bar is 1 mm.

$$R = C t |\sigma_1 - \sigma_2| = 2 C t \sqrt{\left(\frac{\sigma_{xx} - \sigma_{yy}}{2}\right)^2 + \tau_{xy}^2}$$
 (Equation 1)

where x and y are the in-plane directions, σ_{xx} and σ_{yy} are normal stresses, and τ_{xy} is the shear stress. This is based on a plane-stress interpretation that assumes that $\sigma_{zz} = 0$ (i.e., the out-of-plane stress). The maximum and minimum principal stresses are then σ_1 and σ_2 , and t is the thickness of the electrolyte. The stress-optic constant, C, quantifies the stress-induced birefringence in a given material describing the impact that stress has on the refractive index (see Figure S3). C was not previously known for any kind of solid electrolyte. The configuration used to measure C for LLZTO is shown in Figure 3. In this setup, a known concentrated load was applied on either end of a slender beam on which the LLZTO specimen was firmly attached. The stress-optic coefficient was then evaluated with a strain gauge that was mounted next to the specimen. This approach was calibrated with a quartz glass, and then employed to obtain a value of $C = 0.90 \times 10^{-12}$ for the LLZTO. Secondary effects that could play a role in these measurements were assessed with finite element analysis, and complicating effects such as the mismatch between the Poisson ratios of the two materials were shown to have a minimal effect. More information on the calibration is provided in the experimental procedures. Furthermore, variation in the difference in principal stresses across the LLZTO pellet was found to be minimal (Figure S3). After obtaining C, the retardance measurements were then used to obtain the difference in principal stresses with Equation 1.

In principle, the quantitative interpretation of photoelasticity measurements can be compared directly with predicted stress fields for an internally pressurized flaw. This has been done in classical mechanics studies with externally loaded cracks, where the results of photoelasticity experiments are qualitatively similar to the patterns in Figures 1 and 2.^{32–34} It is thus logical to use this type of treatment as an idealized analysis of stresses that are associated with the Li-filled dendrites.

For an idealized straight Griffith crack where a constant internal pressure, p_0 , exerts a normal force on the crack faces, the following result has been obtained for plane stress:³⁸





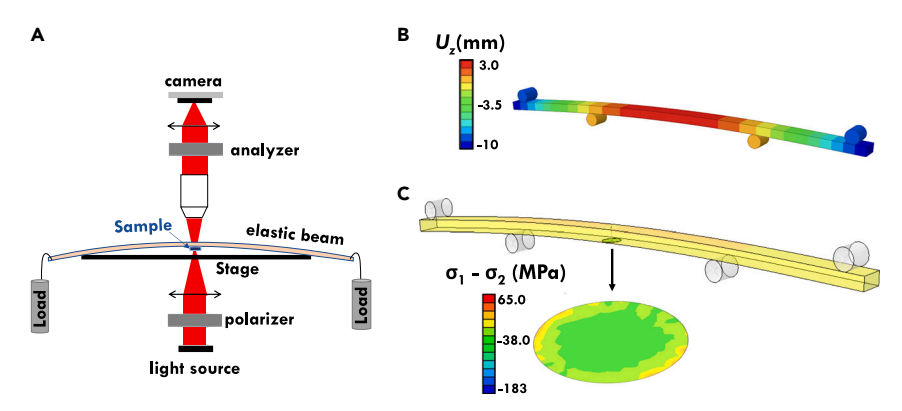


Figure 3. Determining the stress-optic constant of the electrolyte

(A) Calibration setup used in determining the stress-optic constant, *C*, describing the impact of stress on the refractive index for LLZTO. A known load was applied on each end of a slender beam. The beam had a 1 mm diameter through-thickness hole in the center. A 12.7 mm diameter, 0.3 mm thick LLZTO specimen was bonded to the beam, concentric with the hole. A strain gauge was mounted next to the specimen. The retardance signal and the strain were assessed with and without load to determine the stress-optic coefficient.

(B and C) Finite element analysis showing the displacement U_z in the slender beam and the $\sigma_1-\sigma_2$ stress distribution in the LLZTO disk (inset). A homogeneous stress state is present at the central part of the LLZTO disk, which is used for the measurements.

$$\sqrt{\left(\frac{\sigma_{xx} - \sigma_{yy}}{2}\right)^2 + \tau_{xy}^2} \cong p_o \sqrt{\frac{c}{8 r}} \sin \varphi$$
 (Equation 2)

where r is the radial distance from the crack tip at an orientation defined by the transformed angular variable φ , and c is the crack length, which is taken here to be the dendrite length. ³⁸ Inserting the stresses from Equation 2 in Equation 1, produces a spatial distribution of optical retardance that matches the experimental observations. This is clearly seen in the similarity between the results in Figure 4B and both measured and calculated photoelasticity results for well-defined cracks. ^{32–34} Based on this comparison, we conclude that the observed retardance corresponds to a compressive stress field in the LLZTO that is produced by pressure inside of the lithium filament.

To provide a quantitative comparison between the experimental results and Equation 2, better resolution is obtained by considering the orientation with the maximum R intensity (i.e., where the signal-to-noise ratio is the highest). Data for the retardance along this maximal orientation radiating from the tip (roughly normal to the dendrite path) were extracted for the image in Figure 2. These data were used to find the best numerical fit to Equation 2 in the parameter $p_o\sqrt{c}$. This analysis demonstrates that meaningful quantitative comparisons are possible with the type of data that are reported here. The fit corresponds to an average value of $p_o\sqrt{c}=0.78$ MPa m^{1/2}. Similar fits to the other images in Figures 2B–2D give average values of $p_o\sqrt{c}=0.75$, 0.79, and 0.88 MPa m^{1/2} respectively. This consistency shows that the functional form of Equation 2 provides a reasonable interpretation of the experimental measurements (more information is given in the supplemental information).

DISCUSSION

In principle, operando measurements of the optical retardance can be used to monitor the large mechanical stresses that accompany dendrite propagation. The central idea here is that plating-induced pressure in the Li can drive dendritic



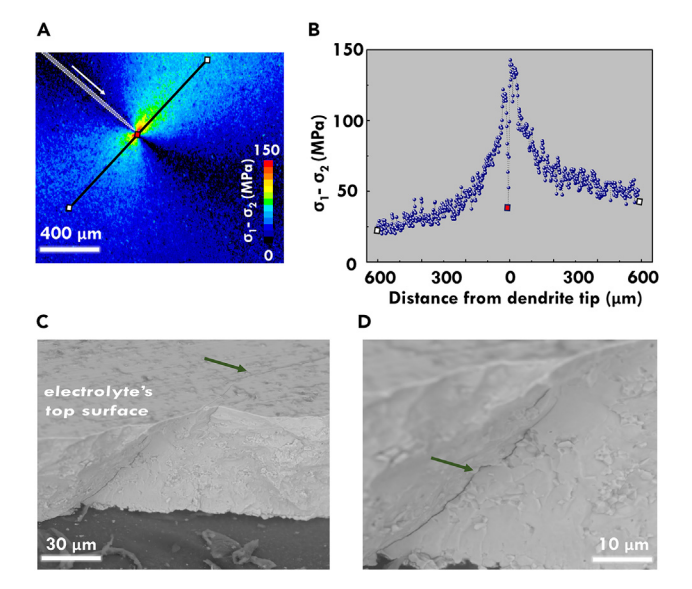


Figure 4. Principal stress profile around the tip of the through-thickness dendrite

(A) Map of the difference in principal stresses ($\sigma_1 - \sigma_2$) in the electrolyte material around the dendrite. The direction of propagation of the dendrite (depicted as a dotted illustration) is indicated by the white arrow.

(B) Difference in principal stresses ($\sigma_1 - \sigma_2$) measured across the line at the tip of the dendrite. The line is perpendicular (90°) to the growth direction. Stress states up to nearly 150 MPa are measured. The stress values follow the distance $^{-1/2}$ scaling expected for a crack in a brittle solid. 38 (C and D) Scanning electron microscope (SEM) images demonstrating the through-thickness nature of the dendritic propagation. The image was taken post-mortem by cleaving an electrolyte and imaging while mounted on a 45° stub. The arrow in (A) shows the dendritic filament where it intersects the top face of the ceramic electrolyte. The dark material beneath the ceramic is carbon adhesive used for mounting the sample in the SEM stage.

growth. ^{15–30} Photoelastic imaging of the stress field near the dendrite clearly provides direct information about this. Our previous work demonstrated that externally applied stresses alter dendrite propagation in LLZTO. ²⁷ However, direct measurements of the stress fields in the vicinity of dendrites have not been reported previously. Imaging of the stress field near the dendrite while plating clearly indicates that substantial pressure buildup occurs in the Li metal. A quantitative interpretation that is based on the analysis presented above must consider several aspects of the experimental configuration that deviate from the assumptions that lead to Equation 2. In particular, the actual dendrites that are shown in Figures 1 and 2 are not as well defined as the idealized crack geometries that are typically used to obtain the standard stress intensity factor, K_I , expressions. ³⁹ Key aspects of these Li-filled dendrites that must be considered when applying Equation 2 include the following.

• This form is based on a 2D interpretation that effectively assumes that the inplane stresses are uniform through the thickness of the electrolyte (i.e., there are no variations in the z direction). To apply this directly to the experiments, there should be minimal relaxation of lithium at the top and bottom surfaces. This is supported by SEM images that show that there is minimal flow of metal out of the filament at these surfaces (e.g., in Figure 4). The presence of multiple dendritic events closely spaced to one another complicates stress quantification due to superposition of the stress fields that are generated in different locations. For this reason, the primary results reported here (Figures 1 and 2) were obtained from an experiment where the dendrite was reasonably far

Matter Article



away from other dendrites. However, this configuration still deviates from the idealized crack geometry that is used to obtain Equation 2.

- To match the 2D plane stress model outlines in Equation 2, the lithium filaments should run uniformly through the thickness of the LLZTO, and the dendrite width should be much smaller than the electrolyte thickness. The fracture surface in Figure 4 indicates that these geometric assumptions are roughly consistent with the experiments. However, one notable deviation is that the dendrite path through the electrolyte is not strictly perpendicular to the top and bottom surfaces of the LLZTO. This may be influenced by the position of the electrodes on the top of the sample and by nonuniformities in the material that are discussed further below.
- Inhomogeneities in the actual LLZTO slab are inevitable, due to microstructural features. While thickness measurements show that the former are relatively small, the latter are an intrinsic feature of these polycrystalline materials that may influence the dendrite path.
- A prerequisite for brittle fracture is that the small-scale yielding condition is satisfied, i.e., only limited amount of plastic deformation takes place around the crack front. Indeed, for the experiments reported here, the small-scale yielding condition is satisfied as $r_p = (1/2\pi)(K_{lc}^2\sigma_y^2) \cong 1$ nm, where r_p is the process zone size, K_{lc} is the fracture toughness of the LLZTO (~1 MPa m^{1/2} based on literature data), and σ_y is the effective yield strength, which is approximated ~10 GPa⁴²
- The pressure inside the filament may be non-uniform due to phenomena such as current focusing at the tip and relaxation due to plastic flow near the base. Recent work also shows evidence for dendrites that are not completely filled with Li (e.g., with empty tips, etc.). 32 With a variable pressure, p(x), Equation 1 can still be applied, with the following: 43

$$\sqrt{\left(\frac{\sigma_{xx} - \sigma_{yy}}{2}\right)^2 + \tau_{xy}^2} \cong \lfloor y \ w''(z) \rfloor$$
 (Equation 3)

where $w(z) = \int_0^c p(x) G(c,x,z) dx$, with G representing the Green's function for a pair of forces of unit magnitude acting along the surface of a finite dendrite of length, c, and the coordinate z = x+iy. Such deviations from the model assumptions may affect the interpretation of the $p_o\sqrt{c}$ values that were obtained by fitting the experimental measurements with Equation 2. The simplest approximation is obtained by taking c as the measured distance from the plating electrode, which gives $p_o \cong 9-11$ MPa. It is tempting to view this as an average pressure, although based on Equation 3 this is only strictly accurate if p(x) is constant. Instead, we believe that it is more appropriate to view p_0 as a lower bound estimate of the internal lithium pressure for several reasons. First, Equation 3 includes contributions from the base of an isolated dendrite. However, as noted above, stresses in the LLZTO may arise due to Li penetration events in other locations, such that the dendrite being examined is not fully isolated and the effective crack length is shorter than c. Stress relaxation from the top and bottom edges and an empty dendrite tip would also imply that the maximum pressure in the dendrite may exceed this estimated p_o value. It is also important to keep in mind that the dendrite lengths of several millimeters in the current experiment are much longer than those that will occur in thinner solid electrolytes that are employed in solid-state batteries. Thus, with a dendrite that is two orders of magnitude smaller (i.e., 70 µm instead of 7 mm), the same K field requires $p_o \sim 100$ MPa based on the classical scaling in Equation 4 for equivalent cell geometry to that studied here.





It is also possible to use the photoelasticity results to evaluate the K field in the vicinity of Li-filled dendrites. The agreement between Equation 2 and the retardance measurements for a Li-filled dendrite show that the observed stress distribution is consistent with the expected K_I field in the vicinity of a crack. This follows directly from the analysis that leads to Equation 2, which gives:³⁹

$$K = \psi p_o \sqrt{c}$$
 (Equation 4)

where ψ is a geometric factor that depends on the crack shape. For a planar crack front, the classical value of $\psi \cong 1.12 \sqrt{\pi}$ gives $K_I = \sim 1.5 - 1.8$ MPa m^{1/2}. This is reasonably close to the measured fracture toughness of LLZTO, 41 and is also consistent with the value of 1.8 MPa $\mathrm{m}^{1/2}$ inferred from the analysis of dendrite deflection measurements in Fincher et al. (using similar LLZTO specimens).²⁷ Furthermore, the $p_o\sqrt{c}$ fitting for the moving dendrite shows that the stress intensity factor, K_l , are similar as the crack front progresses. Our observations show that stresses that develop during dendrite propagation are consistent with those from classical fracture mechanics.32-34

Conclusions

The measurements reported here demonstrate that photoelasticity can be employed to directly quantify and visualize the stresses in LLZTO during electrochemical cycling. This is a new contactless, quantitative methodology that can be used to conduct operando investigations of stress-driven phenomena in solid electrolytes. The results show that operando optical birefringence provides direct information about lithium metal penetration through LLZTO.

Direct measurement of optical retardance provides a direct measure of the compressive stresses near a dendrite. This approach provides the first direct, observation of the stresses that occur around this type of dendrite. The stress distributions and the corresponding stress intensity factor near the lithium dendrite tip match those expected for dendrite propagation²⁷ and for brittle fracture. Future work could include the reconstruction of the full stress tensor around the dendrite tip using inverse 3D photoelasticity, which requires advancements in the experimental setup (e.g., the capability to image the specimen from different angles and achieving higher optical resolution) coupled with extensions in the existing computational frameworks (e.g., via the use of artificial intelligence)^{44–47} for proper interpretation of the results.

In summary, the work reported here provides conclusive evidence that large internal stresses are produced by lithium dendrites in LLZTO at the current densities studied here. The photoelasticity-based characterization platform proposed in this study has the potential to facilitate operando investigations of stress-related failure mechanisms and phenomena, such as environmental cracking effects, ⁴⁸ in battery materials across various length and timescales.

EXPERIMENTAL PROCEDURES

Resource availability

Lead contact

Prof. Christos E. Athanasiou (athanasiou@gatech.edu) will serve as lead contact.

Materials availability

This study did not generate new unique materials.

Data and code availability

All data are available upon reasonable request.

Matter Article



Photoelasticity setup, calibration, and imaging

Stress-induced birefringence was measured using a digital photoelastic system consisting of an optical microscope (Olympus BX51) equipped with a liquid-crystal universal compensator for measuring birefringence (VariLC). The Abrio software provided all the necessary functions for calibration of the LC compensator and retardance measurement acquisition. Further post-processing using ImageJ was then employed for applying false color maps to each measurement, as well as extract retardance, and, therefore, principal stress data. The pixel size for this configuration was $\sim\!1.7~\mu m$. A background retardance value of $\sim\!2.5~nm$ was observed and could be an effect of multiple parameters including from the optical setup itself, from circular dichroism of the ceramic electrolyte, and image capturing parameters. This is typically subtracted by the measured retardance values provided in Figures 1, 2, and 4. The same optical setup without the LC compensator was used to obtain the images in Figure 2A. After cleaving the sample, SEM imaging was performed using PhenomProX while the specimen was mounted on carbon tape (Figure 4C).

Cell preparation, cell assembly, and operando electrochemical plating

Cell preparation and assembly follows that from Fincher et al. ²⁷ The polycrystalline LLZTO was obtained from Toshima Manufacturing (Saitama, Japan) as 1 mm thick, 12.7 mm diameter pellets. LLZTO electrolytes were then mechanically polished to the end thickness specified of ~90 μm , using oil-based 1 μm diamond suspension for the last polishing step. Immediately after polish, the electrolyte disks were transferred into an oven within an Ar-containing glovebox. After the disks were heat treated at 500°C for 3 h, the Li metal/LLZTO interface was formed, and finally the electrolyte disks were removed from the oven. ²⁷ Li metal foil (Alfa Aesar, Ward Hill, MA) was scraped with a steel spatula to produce a clean metal surface. ²⁷ This Li was then cut into 3 mm diameter pads using a biopsy punch. The Li metal pads were immediately adhered to the LLZTO disk, and the resulting assembly was placed into the oven and baked at 250°C for 1 h. Note that only one Li metal electrode is required to grow the dendrites, i.e., we directly plated and grew dendrites without the use of Li metal as a positive electrode (Figures 1A and 1C).

After cell preparation, the specimens were placed in an Ar-filled unit, which is comprised of a Viton O-ring glued on top and bottom side to the surface of the two glass slides (Figure S1). Tungsten probe tips were inserted into the Li metal electrodes to provide an electrical connection to a VMP-3 potentiostat (Biologic, Knoxville, TN). Such experimental design allowed for controlled electrochemical cycling outside the glovebox. As the glass box does not offer long-term protection, the tests were performed within a few hours after the assembly and conducted at room temperature.

Stress-optic calibration for LLZTO using experiments and finite element analysis

A LLZTO disk was fixed to a cantilever bar using Loctite 401 adhesive. The adhesive was allowed to cure for 3 h. For the experiment shown in Figure 3A, a 20 mm thick, 44 mm wide, 600 mm long acrylic bar (McMaster, Elmhurst, IL) was used (Figure S2). A strain gauge was fixed 1 cm from the specimen. Following this, a load of 1 kg on each side of the bar was applied as shown in Figure 3A. Two specimens were used for the measurement and validation of the stress-optic constant: a 300 μ m thick LLZTO and a 160 μ m thick quartz glass slide. To obtain the stress-optic coefficient, C, the relationship between the retardance, R, and maximum principal stress was used as per Equation 1. Taking the direction along the bar's axis as the x direction with the face of the bar in the x-y plane, we treat the sample as being in plane stress





 $(\sigma_{zz}=0)$ and approximating the electrolyte disk as fixed to the bar. The bar is approximated as rigid and possessing only axial strain measured by the strain gauge $(\varepsilon_{meas.})$, giving $\varepsilon_{xy}=0$, $\varepsilon_{yy}=0$, and $\varepsilon_{xx}=\varepsilon_{meas.}$. This implies, from Hooke's law, that:

$$\sigma_1 - \sigma_2 = \sigma_{xx} - \sigma_{yy} = \frac{E}{1+v} \varepsilon_{meas.}$$
 (Equation 6)

By combining Equation 6 with Equation 1:

$$C = \frac{R}{t(\sigma_1 - \sigma_2)} = \frac{1+\nu}{E} \frac{1}{\varepsilon_{\text{meas.}}} \frac{R}{t}$$
 (Equation 7)

For LLZTO, we take $t=300~\mu m$, $\nu=0.25$, E=150~GPa, $\varepsilon_{meas.}=584$ microstrain, and R=23.58 nm for symmetric 1 kg loads. This gives C of $9\times 10^{-13}~Pa^{-1}$ for LLZTO. Similar loading of a glass coverslip ($t=160~\mu m$, E=60~GPa, $\varepsilon_{meas.}=672$ microstrain) yields a C of $6.45\times 10^{-13}~Pa^{-1}$. Based on this calibration we can evaluate the maximum relative error of the retardance measurement using the standard deviation from three measurements with known load. The relative error in retardance is <4% resulting into a maximum error in the difference in principal stresses of $\sim 10~MPa$.

To investigate potential influence from effects such as Poisson contractions, finite element simulations were performed in Abaqus. ⁵⁰ The NIgeom option was enabled during simulation. A 3D finite element analysis of the four-point bending setup of the slender (acrylic) beam with the LLZTO pellet attached at the bottom as shown in Figure 3B. A schematic of the geometry of the simulation domain and respective dimensions is presented in Figures S3 and S4, representative of the experimental setup. A set of four discrete rigid cylindrical supports were introduced, respectively, two at the bottom to provide support of the beam-pellet assembly, and two at the top to replicate the loading from the experimentally applied weights. The acrylic beam and the LLZO pallet are modeled as 3D linear-elastic deformable bodies, meshed with 3D linear reduced-integration brick elements (C3D8R), for a total of 32,385 elements. Under a linear-elastic framework, we prescribe the acrylic beam a Young's modulus of 4.5 GPa and Poisson ratio of 0.37, while the LLZTO pellet is modeled with a Young's modulus of 150 GPa and Poisson ratio of 0.25. 51 A hard contact interaction is enforced in the normal direction to prevent any interpenetration of surfaces upon loading and a surface-to-surface tie constraint is established between the LLZTO and the acrylic beam such that no relative sliding between the bottom surface of the acrylic beam and the top surface of LLZTO pellet can occur. Concentrated loads of 10 N were applied on each rigid cylindrical support on either end of the acrylic beam, consistent with the 1 kg weights attached on the acrylic beam ends during experiments. To prevent rigid body translation of the assembly upon loading, the bottom cylindrical supports are restrained from both translational and rotational motion. Similarly, cylindrical supports on top of the acrylic beam are limited to only downward motion in response to applied loading, with the remaining translational and rotational degrees of freedom restrained.

SUPPLEMENTAL INFORMATION

Supplemental information can be found online at https://doi.org/10.1016/j.matt. 2023.10.014.

ACKNOWLEDGMENTS

C.E.A. and B.W.S. acknowledge funding from NSF (DMR-2124775). C.F. and Y.M.C. acknowledge support from the Mechano-Chemical Understanding of Solid Ion Conductors, an Energy Frontier Research Center funded by the U.S. Department of

Matter Article



Energy, Office of Science, Office of Basic Energy Science, contract DE-SC0023438. C.F. acknowledges funding from the Department of Defense Science and Engineering Graduate Fellowship.

AUTHOR CONTRIBUTIONS

The use of birefringence microscopy to monitor stresses associated with dendrites was conceptualized by C.E.A. The experimental configuration was designed by C.E.A. and C.D.F. Data were acquired by C.D.F. and curated by C.D.F., C.G., and C.E.A. Analysis of the results was conducted by C.E.A., C.D.F., and B.W.S. The first draft of the manuscript was prepared by C.E.A., C.D.F., and B.W.S. All authors contributed to review and editing of the manuscript.

DECLARATION OF INTERESTS

The authors declare no competing interests.

Received: April 22, 2023 Revised: July 20, 2023 Accepted: October 12, 2023 Published: November 7, 2023

REFERENCES

- Albertus, P., Babinec, S., Litzelman, S., and Newman, A. (2017). Status and challenges in enabling the lithium metal electrode for highenergy and low-cost rechargeable batteries. Nat. Energy 3, 16–21.
- Hatzell, K.B., Chen, X.C., Cobb, C.L., Dasgupta, N.P., Dixit, M.B., Marbella, L.E., McDowell, M.T., Mukherjee, P.P., Verma, A., Viswanathan, V., et al. (2020). Challenges in lithium metal anodes for solid-state batteries. ACS Energy Lett. 5, 922–934.
- Kim, K.J., and Rupp, J.L.M. (2020). All ceramic cathode composite design and manufacturing towards low interfacial resistance for garnetbased solid-state lithium batteries. Energy Environ. Sci. 13, 4930–4945.
- 4. Zhao, Y., Stein, P., Bai, Y., Al-Siraj, M., Yang, Y., and Xu, B.-X. (2019). A review on modeling of electro-chemo-mechanics in lithium-ion batteries. J. Power Sources 413, 259–283.
- McDowell, M.T., Cortes, F.J.Q., Thenuwara, A.C., and Lewis, J.A. (2020). Toward High-Capacity Battery Anode Materials: Chemistry and Mechanics Intertwined. Chem. Mater. 32, 8755–8771.
- 6. Wang, M.J., Kazyak, E., Dasgupta, N.P., and Sakamoto, J. (2021). Transitioning solid-state batteries from lab to market: Linking electrochemo-mechanics with practical considerations. Joule *5*, 1371–1390.
- Athanasiou, C.E., Liu, X., Jin, M.Y., Nimon, E., Visco, S., Lee, C., Park, M., Yun, J., Padture, N.P., Gao, H., and Sheldon, B.W. (2022). Ratedependent deformation of amorphous sulfide glass electrolytes for solid-state batteries. Cell Reports Physical Science 3, 100845.
- 8. Famprikis, T., Canepa, P., Dawson, J.A., Islam, M.S., and Masquelier, C. (2019). Fundamentals of inorganic solid-state electrolytes for batteries. Nat. Mater. 18, 1278–1291.

- Athanasiou, C.E., Jin, M.Y., Ramirez, C., Padture, N.P., and Sheldon, B.W. (2020). Hightoughness inorganic solid electrolytes via the use of reduced graphene oxide. Matter 3, 212–229.
- Vishnugopi, B.S., Kazyak, E., Lewis, J.A., Nanda, J., McDowell, M.T., Dasgupta, N.P., and Mukherjee, P.P. (2021). Challenges and opportunities for fast charging of solid-state lithium metal batteries. ACS Energy Lett. 6, 3734–3749.
- 11. Koerver, R., Zhang, W., de Biasi, L., Schweidler, S., Kondrakov, A.O., Kolling, S., Brezesinski, T., Hartmann, P., Zeier, W.G., and Janek, J. (2018). Chemo-mechanical expansion of lithium electrode materials-on the route to mechanically optimized all-solid-state batteries. Energy Environ. Sci. 11, 2142–2158.
- Singh, A., and Pal, S. (2022). Chemomechanical modeling of inter-and intragranular fracture in heterogeneous cathode with polycrystalline particles for lithium-ion battery. J. Mech. Phys. Solid. 163, 104839.
- Naik, K.G., Vishnugopi, B.S., and Mukherjee, P.P. (2022). Kinetics or transport: whither goes the solid-state battery cathode? ACS Appl. Mater. Interfaces 14, 29754–29765.
- Sharafi, A., Meyer, H.M., Nanda, J., Wolfenstine, J., and Sakamoto, J. (2016). Characterizing the Li-Li7La3Zr2O12 interface stability and kinetics as a function of temperature and current density. J. Power Sources 302, 135–139.
- Porz, L., Swamy, T., Sheldon, B.W., Rettenwander, D., Frömling, T., Thaman, H.L., Berendts, S., Uecker, R., Carter, W.C., and Chiang, Y.-M. (2017). Mechanism of lithium metal penetration through inorganic solid electrolytes. Adv. Energy Mater. 7, 1701003.

- Swamy, T., Park, R., Sheldon, B.W., Rettenwander, D., Porz, L., Berendts, S., Uecker, R., Carter, W.C., and Chiang, Y.-M. (2018). Lithium metal penetration induced by electrodeposition through solid electrolytes: example in single-crystal Li₆La₃ZrTaO₁₂ garnet. J. Electrochem. Soc. 165, A3648–A3655.
- Shen, F., Dixit, M.B., Xiao, X., and Hatzell, K.B. (2018). Effect of pore connectivity on Li dendrite propagation within LLZO electrolytes observed with synchrotron X-ray tomography. ACS Energy Lett. 3, 1056–1061.
- Klinsmann, M., Hildebrand, F.E., Ganser, M., and McMeeking, R.M. (2019). Dendritic cracking in solid electrolytes driven by lithium insertion. J. Power Sources 442, 227226.
- Shishvan, S.S., Fleck, N.A., McMeeking, R.M., and Deshpande, V.S. (2020). Dendrites as climbing dislocations in ceramic electrolytes: Initiation of growth. J. Power Sources 456, 227989.
- Kazyak, E., Garcia-Mendez, R., LePage, W.S., Sharafi, A., Davis, A.L., Sanchez, A.J., Chen, K.-H., Haslam, C., Sakamoto, J., and Dasgupta, N.P. (2020). Li penetration in ceramic solid electrolytes: operando microscopy analysis of morphology, propagation, and reversibility. Matter 2, 1025–1048.
- 21. Qi, Y., Ban, C., and Harris, S.J. (2020). A new general paradigm for understanding and preventing Li metal penetration through solid electrolytes. Joule 4, 2599–2608.
- Barroso-Luque, L., Tu, Q., and Ceder, G. (2020). An analysis of solid-state electrodeposition-induced metal plastic flow and predictions of stress states in solid ionic conductor defects.
 J. Electrochem. Soc. 167, 020534.
- Hao, S., Daemi, S.R., Heenan, T.M., Du, W., Tan, C., Storm, M., Rau, C., Brett, D.J., and Shearing, P.R. (2021). Tracking lithium





- penetration in solid electrolytes in 3D by in-situ synchrotron X-ray computed tomography. Nano Energy *82*, 105744.
- Ning, Z., Jolly, D.S., Li, G., De Meyere, R., Pu, S.D., Chen, Y., Kasemchainan, J., Ihli, J., Gong, C., Liu, B., et al. (2021). Visualizing platinginduced cracking in lithium-anode solidelectrolyte cells. Nat. Mater. 20, 1121–1129.
- 25. Kinzer, B., Davis, A.L., Krauskopf, T., Hartmann, H., LePage, W.S., Kazyak, E., Janek, J., Dasgupta, N.P., and Sakamoto, J. (2021). Operando analysis of the molten Li| LLZO interface: understanding how the physical properties of Li affect the critical current density. Matter 4, 1947–1961.
- Hao, S., Bailey, J.J., Iacoviello, F., Bu, J., Grant, P.S., Brett, D.J.L., and Shearing, P.R. (2021). 3D imaging of lithium protrusions in solid-state lithium batteries using X-ray computed tomography. Adv. Funct. Mater. 31, 2007564.
- Fincher, C.D., Athanasiou, C.E., Gilgenbach, C., Wang, M., Sheldon, B.W., Carter, W.C., and Chiang, Y.-M. (2022). Controlling dendrite propagation in solid-state batteries with engineered stress. Joule 6, 2794–2809.
- 28. Vishnugopi, B.S., Dixit, M.B., Hao, F., Shyam, B., Cook, J.B., Hatzell, K.B., and Mukherjee, P.P. (2022). Mesoscale interrogation reveals mechanistic origins of lithium filaments along grain boundaries in inorganic solid electrolytes. Adv. Energy Mater. 12, 2102825.
- Zhao, J., Tang, Y., Dai, Q., Du, C., Zhang, Y., Xue, D., Chen, T., Chen, J., Wang, B., Yao, J., et al. (2022). In situ observation of Li depositioninduced cracking in garnet solid electrolytes. Energy & Environ. Materials 5, 524–532.
- 30. Bistri, D., and Di Leo, C.V. (2023). A continuum electro-chemo-mechanical gradient theory coupled with damage: Application to Li-metal filament growth in all-solid-state batteries.

 J. Mech. Phys. Solid. 174, 105252.
- Cloud, G. (1998). Optical Methods of Engineering Analysis (Cambridge University Press)
- 32. Nigam, H., and Shukla, A. (1988). Comparison of the techniques of transmitted caustics and

- photoelasticity as applied to fracture. Exp. Mech. 28, 123–131.
- Patil, P., Vyasarayani, C.P., and Ramji, M. (2017). Linear least squares approach for evaluating crack tip fracture parameters using isochromatic and isoclinic data from digital photoelasticity. Opt Laser. Eng. 93, 182–194.
- Ham, S.-M., and Kwon, T.-H. (2020). Photoelastic observation of toughness-dominant hydraulic fracture propagation across an orthogonal discontinuity in soft, viscoelastic layered formations. Int. J. Rock Mech. Min. Sci. 134, 104438.
- Vasudevan, T.N., and Krishnan, R.S. (1972).
 Dispersion of the stress-optic coefficient in glasses. J. Phys. D Appl. Phys. 5, 2283–2287.
- Athanasiou, C.-E., and Bellouard, Y. (2015). A monolithic micro-tensile tester for investigating silicon dioxide polymorph micromechanics, fabricated and operated using a femtosecond laser. Micromachines 6, 1365–1386.
- McMillen, B., Athanasiou, C., and Bellouard, Y. (2016). Femtosecond laser direct-write waveplates based on stress-induced birefringence. Opt Express 24, 27239–27252.
- Sneddon, I.N. (1946). The distribution of stress in the neighbourhood of a crack in an elastic solid. Proceedings of the Royal Society of London. Series A. Mathematical and Physical Sciences 187, 229–260.
- Lawn, B.R., Wilshaw, T.R., and Rice, J.R. (1977). Fracture of Brittle Solids (Cambridge Solid State Science Series).
- 40. Rice, J.R. (1974). Limitations to the small scale yielding approximation for crack tip plasticity. J. Mech. Phys. Solid. 22, 17–26.
- Wolfenstine, J., Jo, H., Cho, Y.-H., David, I.N., Askeland, P., Case, E.D., Kim, H., Choe, H., and Sakamoto, J. (2013). A preliminary investigation of fracture toughness of Li7La3Zr2O12 and its comparison to other solid Li-ionconductors. Mater. Lett. 96, 117–120.
- 42. Athanasiou, C.E., Liu, X., Zhang, B., Cai, T., Ramirez, C., Padture, N.P., Lou, J., Sheldon,

- B.W., and Gao, H. (2023). Integrated simulation, machine learning, and experimental approach to characterizing fracture instability in indentation pillar-splitting of materials. J. Mech. Phys. Solid. 170, 105092.
- Glinka, G. (1996). Development of weight functions and computer integration procedures for calculating stress intensity factors around cracks subjected to complex stress fields. Stress and Fatigue-Fracture Design, Petersburg Ontario, Canada, Progress Report 1, 1.
- Guo, K., Yang, Z., Yu, C.H., and Buehler, M.J. (2021). Artificial intelligence and machine learning in design of mechanical materials. Mater. Horiz. 8, 1153–1172.
- Liu, X., Athanasiou, C.E., Padture, N.P., Sheldon, B.W., and Gao, H. (2021). Knowledge extraction and transfer in data-driven fracture mechanics. Proc. Natl. Acad. Sci. USA 118, e2104765118.
- Liu, X., Athanasiou, C.E., Padture, N.P., Sheldon, B.W., and Gao, H. (2020). A machine learning approach to fracture mechanics problems. Acta Mater. 190, 105–112.
- Karapiperis, K., and Kochmann, D.M. (2023). Prediction and control of fracture paths in disordered architected materials using graph neural networks. Commun. Eng. 2, 32.
- Nazir, S.I., Athanasiou, C.E., and Bellouard, Y. (2022). On the behavior of uniaxial static stress loaded micro-scale fused silica beams at room temperature. J. Non-Cryst. Solids X 14, 100083.
- 49. Oldenbourg, R. (2005). Polarization microscopy with the LC-PolScope. In Live Cell Imaging (A laboratory manual), pp. 205–237.
- Abaqus. (2019). Abaqus Reference Manuals, Version 6.10 (Providence, RI: Dassault Systemes Simulia).
- Yu, S.Y., Wang, H.M., Garcia-Mendez, R., Herbert, E., Dudney, N.J., Wolfenstine, J.B., Sakamoto, J., and Siegel, D.J. (2016). Elastic properties of the solid electrolyte Li7La3Zr2O12 (LLZO). Regen. Biomater. 3, 197–203.